PAPER

Synergistic effect of ZIF-8 and NiCo$_2$O$_4$ toward efficient performance for urea electrooxidation

Fowzia S. Alamro,[a] Mahmoud A. Hefnawy, [ID] *[b] Nada S. Al-Kadhi,[a] Hoda A. Ahmed[c] and Shymaa S. Medany [ID] *[b]

Efficient and stable electrocatalysts for urea electrooxidation are essential for sustainable energy generation and wastewater treatment. In this study, a hybrid nanocomposite of nickel cobaltite (NiCo$_2$O$_4$, NCO) and zeolitic imidazolate framework-8 (ZIF-8), denoted NCO-ZIF-8B, was synthesized using ZIF-8 prepared by a conventional hydrothermal method, followed by low-temperature annealing. Structural and morphological analyses using XRD, SEM, EDX, IR, UV-vis, and TGA confirmed the formation of a porous NCO-ZIF-8B architecture with uniform nanoparticle distribution. Electrochemical measurements in 1.0 M NaOH containing 1.0 M urea demonstrated superior performance of NCO-ZIF-8B compared to pristine NCO. Additionally, NCO-ZIF-8B achieved a peak current density of 38.3 mA cm^{-2} at 0.558 V *vs.* Ag/AgCl, a lower onset potential of 0.35 V, and a Tafel slope of 47 mV dec^{-1}, outperforming pristine NCO (I_P = 21.8 mA cm^{-2}, onset potential = 0.41 V, Tafel slope = 69 mV dec^{-1}). The enhanced activity is attributed to increased surface area, improved conductivity, and a higher density of active redox sites. The results highlight NCO-ZIF-8B as a promising electrocatalyst for efficient urea electrooxidation.

1 Introduction

Energy drives all natural and human-made processes, powering everything from biological functions to advanced technologies.[1,2] It exists in various forms, such as kinetic, potential, thermal, and electrical, and can be transformed from one type to another. Sustainable energy production is essential for meeting global demands while preserving environmental balance.[3–5] Sustainable energy sources including solar, wind, hydrogen, geothermal, and biomass rely on naturally replenished resources. These technologies significantly reduce greenhouse gas emissions and promote a cleaner, more resilient energy future.[6–10] Renewable energy comes from naturally replenished sources such as solar, wind, hydro, geothermal, and biomass. Solar panels capture sunlight, wind turbines harness moving air, and hydroelectric plants use flowing water.[11–13] Fuel cells are electrochemical devices that convert the chemical energy of a fuel, typically hydrogen, directly into electricity, heat, and water.[14,15] Unlike combustion engines, they operate without burning fuel, resulting in higher efficiency and lower emissions.[16,17]

Urea fuel cells generate electricity by electrooxidizing urea-rich solutions, producing electrons, protons, nitrogen, and carbon dioxide.[18,19] They combine clean energy generation with wastewater treatment, offering a low-cost, sustainable option for decentralized power and waste-to-energy applications.[20,21]

Zeolitic imidazolate frameworks (ZIFs) are a subclass of MOFs composed of transition metal ions (*e.g.*, Zn^{2+}, Co^{2+}) linked by imidazolate ligands.[22,23] Combining the versatility of MOFs with the stability of zeolites, ZIFs feature high porosity, large surface areas, and excellent thermal and chemical stability. ZIF-8 is one of the most studied ZIFs owing to its stability and well-defined polyhedral morphology.[24–26] Due to excellent chemical and thermal stability make it suitable for diverse applications,[27,28] including gas storage and separation (*e.g.*, CO$_2$ capture and H$_2$ storage),[29–31] adsorption of heavy metals and dyes from wastewater,[32,33] heterogeneous catalysis (such as CO oxidation and organic transformations),[34,35] and electrochemical energy storage or conversion.[36–38] ZIF-8 is also widely employed as a template or host matrix for hybrid nanocomposites, where its porosity and structural robustness enhance performance in energy and environmental technologies.[39]

Sreekanth *et al.* synthesized a Co$_3$O$_4$ electrocatalyst *via* annealing ZIF-67 and investigated its performance for the urea oxidation reaction (UOR). Electrochemical studies showed that the ZIF-67-derived Co$_3$O$_4$ exhibited a lower Tafel slope (134 mV dec^{-1}), higher electrochemically active surface area, and greater current density compared to pristine ZIF-67. Chronoamperometric analysis further revealed excellent stability during prolonged operation, highlighting the potential of ZIF-derived

[a]Department of Chemistry, College of Science, Princess Nourah Bint Abdulrahman University, P.O. Box 84428, Riyadh 11671, Saudi Arabia

[b]Chemistry Department, Faculty of Science, Cairo University, Giza, Egypt. E-mail: shymaasamir80@cu.edu.eg; maahefnawy@gmail.com; maadel@cu.edu.eg

[c]Department of Chemistry, College of Science in Yanbu, Taibah University, Yanbu Governorate, Saudi Arabia

Co_3O_4 as a low-cost and efficient electrocatalyst for UOR and related energy applications.[40]

Spinel oxides (AB_2O_4) are versatile materials with divalent (A) and trivalent (B) metal ions distributed among tetrahedral and octahedral sites within a cubic oxygen lattice.[41–43] Their flexible structure enables extensive cation substitution, giving rise to tunable physicochemical properties such as high stability, multiple redox states, and enhanced electrical conductivity. These features make spinel oxides attractive for electrocatalysis, energy storage, and sensing. In particular, bimetallic spinels like $NiCo_2O_4$, $ZnCo_2O_4$, and $MnCo_2O_4$ show superior electrochemical activity over monometallic oxides attributed to synergistic interactions that enhance electron transfer and active site availability.[44–47]

The combination of spinel oxides with ZIF-8 creates a synergistic catalyst, where spinel oxides provide abundant redox-active sites and ZIF-8 enhances surface area, porosity, and charge transfer. This integration improves active site accessibility, reduces overpotential, and enhances stability, leading to superior catalytic performance.[48–50]

In this work, spinel oxide ($NiCo_2O_4$) and ZIF-8 were prepared and mixed together to enhance the activity toward efficient electrooxidation of urea in alkaline medium. The prepared materials were first characterized using several analytical techniques to confirm the structure of the prepared materials. Then the activity of materials was characterized by electrochemical techniques like cyclic voltammetry, chronoamperometry, and electrochemical impedance spectroscopy.

2 Experimental section

2.1. Preparation of ZIF-8

ZIF-8 was also synthesized *via* a conventional hydrothermal method. In this approach, 2.97 g of zinc nitrate hexahydrate ($Zn(NO_3)_2 \cdot 6H_2O$) and 6.48 g of 2-methylimidazole (MIP) were dissolved separately in 50 mL of methanol each, maintaining a molar ratio of MIP to Zn^{2+} of 8 : 1. The zinc solution was slowly added to the ligand solution under stirring to ensure homogeneous mixing, and the resulting mixture was transferred into a Teflon-lined autoclave and heated at 120 °C for 12 h. After cooling to room temperature, the formed ZIF-8 crystals were collected by centrifugation, and washed several times with methanol to remove unreacted precursors, then dried under vacuum at 70 °C for 12 h, yielding highly crystalline and uniform ZIF-8 suitable for the next step.

2.2. Preparation of $NiCo_2O_4$ spinel oxide

$NiCo_2O_4$ was synthesized *via* a co-precipitation method followed by calcination. Briefly, 2.908 g of $Ni(NO_3)_2 \cdot 6H_2O$ (0.01 mol) and 5.821 g of $Co(NO_3)_2 \cdot 6H_2O$ (0.02 mol) were dissolved in 100 mL of deionized water under magnetic stirring to obtain a homogeneous solution. Ammonium hydroxide (28% NH_4OH) was then added dropwise until the pH reached ~9.0, forming a greenish-brown precipitate. The suspension was stirred for an additional 60 min at room temperature, and the resulting solid was collected by centrifugation, and washed several times with

deionized water and ethanol, then dried at 80 °C overnight. Finally, the dried precursor was calcined in air at 700 °C for 3 h (heating rate: 5 °C min^{-1}) to obtain crystalline $NiCo_2O_4$ spinel oxide.

2.3. Electrode preparation

The electrodes were prepared by mixing $NiCo_2O_4$ (NCO) with different amounts of ZIF-8 to obtain composites containing 10, 20, 30, and 40 wt% ZIF-8, designated as NCO-ZIF-8A, NCO-ZIF-8B, NCO-ZIF-8C, and NCO-ZIF-8D, respectively. For each composition, a catalyst ink with a concentration of 20 mg mL^{-1} was prepared in a water/isopropanol solution (1 : 1, v/v) containing 5 µL of 5 wt% Nafion as a binder, followed by ultrasonication for 30 min to form a uniform suspension. A volume of 20 µL of the resulting ink was drop-cast onto a polished glassy carbon electrode (0.0707 cm^2), giving a catalyst loading of about 0.4 mg. The modified electrodes were dried under ambient conditions and subsequently activated electrochemically in alkaline electrolyte before further electrochemical measurements.

2.4. Electrochemical measurement

The electrochemical measurements were performed in a conventional three-electrode cell using a Pt wire as the counter electrode and an Ag/AgCl/KCl (saturated) electrode as the reference, while the modified GC/NCO-ZIF-8, and GC/Pristine NCO electrodes served as the working electrode. Cyclic voltammetry (CV), Linear sweep voltammetry (LSV), Constant potential chronoamperometry (CA), and electrochemical impedance spectroscopy (EIS) were conducted on an Autolab PGSTAT128N potentiostat/galvanostat. The EIS data were obtained by applying a sinusoidal AC perturbation of 10 mV over a frequency range of 1×10^4 to 0.1 Hz, and the spectra were fitted using the Nova software package (Version 2.1, Metrohm Autolab, Utrecht, Netherlands). All potentials reported in this study are referenced to the Ag/AgCl/KCl (saturated) electrode.

3 Results and discussion

3.1. Characterization

The chemical structure of the prepared materials was confirmed using powder X-ray diffraction (XRD).

The XRD patterns of pristine nickel cobalt oxide (NCO), ZIF-8, and the NCO-ZIF-8 composite are shown in Fig. 1a. For pure NCO, the diffraction peaks located at $2\theta \approx 30.6°$ (220), 36.4° (311), 44.3° (400), 58.6° (511), and 65.7° (440) can be indexed to the cubic spinel $NiCo_2O_4$ phase (JCPDS card no. 20-0781), confirming the successful formation of crystalline NCO.[51,52] The relatively sharp and intense reflections further indicate the high crystallinity of the oxide phase.

For pure ZIF-8, the XRD pattern exhibits characteristic diffraction peaks at 7.3° (011), 10.3° (002), 12.9° (112), 14.7° (022), 16.6° (013), and 18.2° (222), which are consistent with the sodalite-type crystalline framework of ZIF-8 (JCPDS #62-1030).[53,54] These sharp reflections confirm the successful
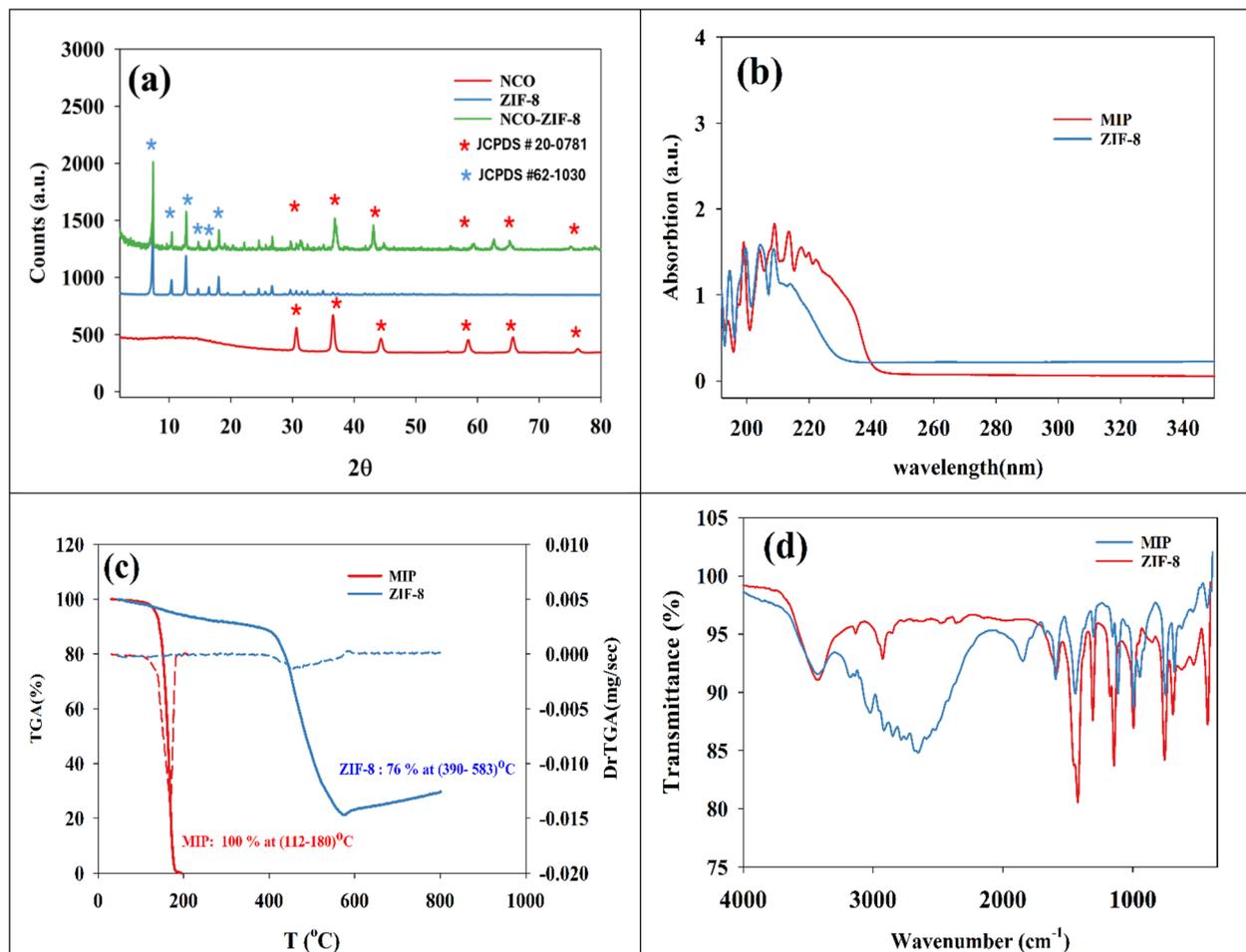
Fig. 1 (a) XRD for 2-methyl ZIF-8, NCO, NCO-ZIF-8, (b) UV-vis, (c) TGA, (d) FT-IR for MIP and ZIF-8.

synthesis of highly crystalline ZIF-8 and are in good agreement with previously reported data.

The NCO-ZIF-8 composite exhibits both sets of characteristic peaks, confirming the coexistence of the $NiCo_2O_4$ spinel structure and the ZIF-8 framework without any additional impurity phases. A slight reduction in the intensity of the ZIF-8 peaks is observed in the composite, which can be attributed to the uniform distribution of NCO nanoparticles on the ZIF-8 surface and partial coverage of its crystal facets. In addition, the NCO reflections in the composite appear slightly broadened compared to those of pristine NCO, particularly (311) and (400) planes, indicating a decrease in crystallite size and possible lattice distortion induced by the strong interfacial interaction between NCO and the ZIF-8 framework. These results confirm the successful integration of NCO with ZIF-8, where ZIF-8 serves as a porous support that disperses NCO nanoparticles and suppresses their agglomeration.

The UV-vis spectra of MIP and ZIF-8 are presented in Fig. 1b. The spectrum of pure 2-methylimidazole shows a strong absorption band at $\sim$220 nm, which can be assigned to the $\pi \rightarrow \pi^*$ electronic transition of the imidazole aromatic ring. A weaker shoulder near 270–280 nm can be attributed to n $\rightarrow \pi^*$

transitions associated with the lone pair electrons of the nitrogen atoms in the imidazole moiety.

Upon the formation of ZIF-8, the absorption features shift due to the coordination of Zn^{2+} ions with the nitrogen atoms of 2-methylimidazole. The ZIF-8 spectrum exhibits a broad absorption edge in the range of 240–260 nm, which is significantly different from that of the free ligand, confirming successful framework formation. The disappearance (or suppression) of the n $\rightarrow \pi^*$ band around 270 nm also supports the consumption of free imidazole groups upon coordination with Zn^{2+}.[55,56]

The observed shift in the absorption edge reflects the modification of the electronic structure and charge transfer properties after Zn–N coordination. This improved electronic coupling facilitates faster electron transport within the framework. Therefore, the DRS results indicate that ZIF-8 possesses favorable optical and electronic characteristics that contribute to its enhanced electrochemical activity.

Fig. 1c shows the TGA and DTG curves of MIP and ZIF-8. The TGA profile of 2-methylimidazole reveals a single, sharp weight loss step of nearly 100% between 112 and 180 °C, which is attributed to the complete volatilization/decomposition of the organic ligand, as confirmed by the corresponding DTG peak. In

contrast, ZIF-8 exhibits markedly higher thermal stability, with only a slight weight loss below 150 °C due to the removal of adsorbed water or residual solvents, followed by a major decomposition step in the range of 390–583 °C, during which approximately 76% of the framework weight is lost. This step corresponds to the breakdown of the imidazolate linkers and the collapse of the framework, leaving about 24% residual mass, likely related to zinc oxide. The DTG curves further emphasize the sharp degradation of 2-methylimidazole compared to the broader, high-temperature decomposition of ZIF-8, demonstrating the stabilizing effect of Zn–N coordination in the framework.

The superior thermal stability of ZIF-8 ensures structural integrity during electrochemical measurements, preventing framework collapse under operational conditions. The strong Zn–N coordination enhances durability and maintains the accessibility of active sites. Hence, the TGA results confirm that ZIF-8 possesses the robustness required for stable and reproducible electrochemical performance.

The functional groups of both MIP and ZIF-8 were characterized by FT-IR spectroscopy. As represented in Fig. 1d, the FTIR spectrum of 2-methylimidazole shows a peak at 3144 cm^{-1} corresponding to the N–H stretching vibration,[57] while the methyl group at the 2-position is confirmed by the C–H stretching at 2943 cm^{-1} and the CH$_3$ bending at 1465 cm^{-1}.[58] Ring vibrations are observed at 1617 cm^{-1} for C=N stretching with C–N stretching at 1296 cm^{-1}, confirming the intact imidazole structure.[59–61] In the FTIR spectrum of ZIF-8, coordination of Zn^{2+} with the imidazolate linker is evidenced by the C=N stretching at 1591 cm^{-1}, C–N stretching at 1161 cm^{-1}, and out-of-plane C–H bending at 998 cm^{-1}, while Zn–N stretching appears around 417 cm^{-1}.[62–65] Comparison of the spectra shows that the imidazole linker is preserved in ZIF-8, with characteristic shifts due to coordination with zinc ions, confirming the successful formation of the ZIF-8 framework from 2-methylimidazole.

The strong Zn–N coordination and preserved imidazolate framework ensure structural robustness and stable electronic pathways during electrochemical processes. These well-defined functional groups facilitate efficient charge transfer between the active sites and electrolyte. Consequently, the FTIR results support the enhanced electrochemical stability and activity of the synthesized ZIF-8-based materials.

The N$_2$ adsorption–desorption isotherms (see Fig. 2a and b) were employed to investigate the surface area and porosity characteristics of the synthesized NCO and NCO-ZIF-8 materials. The Brunauer–Emmett–Teller (BET) analysis clearly reveals that the incorporation of the ZIF-8 framework significantly modifies the porosity characteristics of the base material. The NCO sample, represented in Fig. 2a, exhibits a relatively low specific surface area of 42.18 m^2 g^{-1} and is predominantly microporous. Such a pore structure is typical of high-selectivity adsorbents, where physisorption primarily occurs through strong pore-filling interactions. In contrast, the NCO-ZIF-8 composite (Fig. 2b) displays a surface area nearly twice that of NCO, reaching 94.8 m^2 g^{-1}. This pronounced transformation suggests that the ZIF-8 component was incorporated in a manner that produced large, loosely packed aggregates or meso/macro-scale voids between composite particles, thereby markedly increasing the total pore volume (0.158 cm^3 g^{-1} for NCO-ZIF-8 vs. 0.127 cm^3 g^{-1} for NCO). Additionally, the NCO-ZIF-8 composite would be advantageous for electrochemical oxidation processes, where enhanced porosity facilitates efficient mass transport, electrolyte penetration, and the rapid diffusion of reactants and products within the electrode structure.

The morphological features of the prepared materials were examined using SEM, as shown in Fig. 3. Pristine ZIF-8 (Fig. 3a) displays a uniform nanocube-like structure with smooth surfaces and well-defined edges. The nanocubes are relatively homogeneous in size and exhibit good dispersion, confirming the successful formation of ZIF-8 crystals. The well-ordered morphology and intrinsic microporosity of ZIF-8 provide a large surface area, abundant adsorption sites, and excellent structural stability. After the incorporation of NCO, the composite (NCO-ZIF-8, Fig. 3b) retains the polyhedral
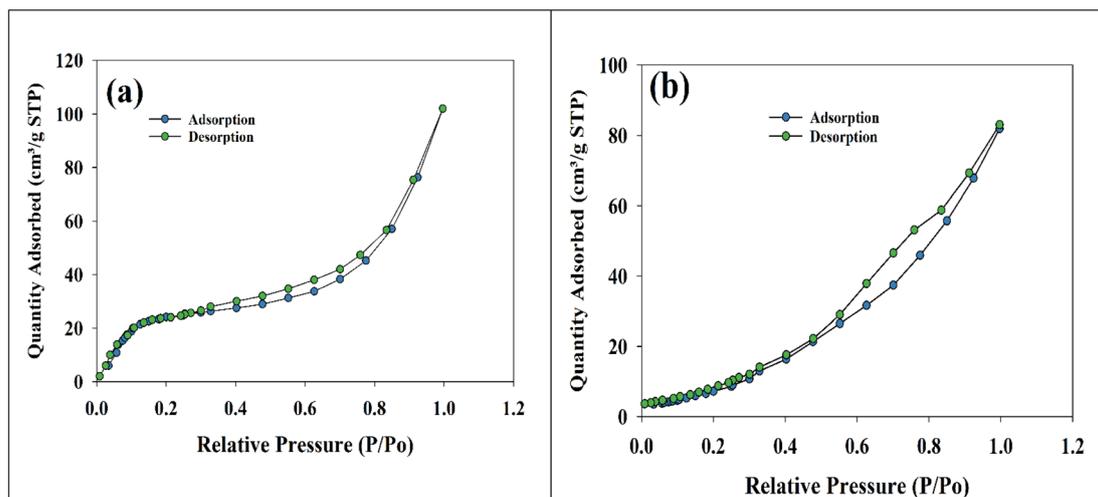

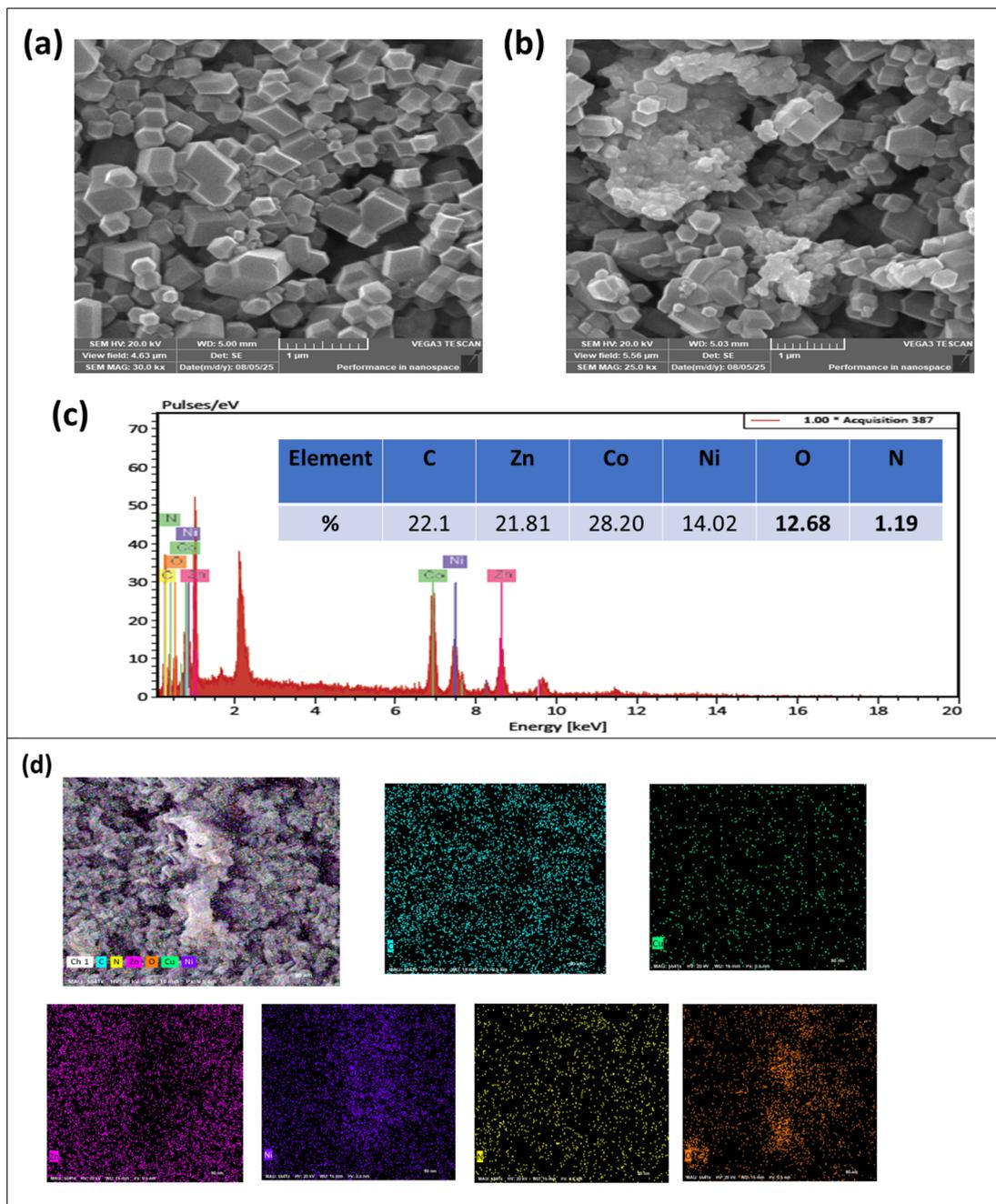**Fig. 2** BET for (a)NCO, (b)NCO-ZIF-8.

Fig. 3 SEM of (a) ZIF-8, and (b) NCO–ZIF-8B. (c) EDX. (d) Elemental mapping.

morphology of ZIF-8; however, numerous NCO nanoparticles are clearly observed to be anchored on the ZIF-8 surface. The decoration of ZIF-8 nanocubes with NCO nanoparticles not only increases the surface roughness but also enhances the interfacial contact, thereby combining the high porosity of ZIF-8 with the superior conductivity and redox activity of NCO, which is expected to improve the overall electrochemical/adsorptive performance of the hybrid material. The elemental composition of the NCO-ZIF-8 composite was further investigated by energy-dispersive X-ray spectroscopy (EDX), as shown in Fig. 3c. The spectrum reveals the presence of C, N, and Zn elements

originating from the ZIF-8 framework, together with Ni, Co, and O signals corresponding to the NCO nanoparticles. The coexistence of these elements confirms the successful decoration of ZIF-8 nanocubes with NCO (please see inset Table in Fig. 3c). The elemental mapping of the NCO-ZIF-8 composite (see Fig. 3d) further confirms the homogeneous distribution of the constituent elements. The components C, N, and Zn are uniformly dispersed, verifying the well-preserved ZIF-8 framework, while Ni, Co, and O are evenly distributed over the ZIF-8 nanocubes, demonstrating the successful anchoring of NCO nanoparticles. This uniform dispersion of active components is

advantageous as it maximizes the accessible active sites, improves interfacial contact, and ensures efficient synergistic interactions between ZIF-8 and NCO within the hybrid structure.

The intimate interfacial contact between NCO and ZIF-8 facilitates rapid charge transfer and ion diffusion during electrochemical reactions. The well-dispersed NCO nanoparticles ensure the exposure of abundant redox-active sites, which enhances the overall electrocatalytic activity. Therefore, the observed morphological characteristics directly support the improved electrochemical behavior discussed in the following sections.

3.2. Elctrochemical urea oxidation

The electrochemical activity of the modified NCO-ZIF-8 electrodes was evaluated by cyclic voltammetry (CV) in 1.0 M urea and 1.0 M NaOH solution. Since the activation of nickel-based electrodes is a crucial step in urea electrooxidation, an activation procedure was employed to enhance their performance. This treatment leads to the formation of a highly active nickel oxyhydroxide (NiOOH) phase, which serves as the main electrocatalytically active species. The activation was carried out by repeated CV (50 cycles) at a scan rate of 200 mV s^{-1} in 1.0 M NaOH. During successive potential sweeps, the continuous formation of NiOOH results in a progressive increase in current response. As the number of cycles increases, the NiOOH layer grows thicker, driven by the presence of OH$^-$ ions that promote the reversible transformation between Ni(OH)$_2$ and NiOOH.

Fig. 4a shows CVs of the NCO-ZIF-8B electrode in 1.0 M NaOH at scan rates ranging from 5 to 100 mV s^{-1} to evaluate its redox behavior and charge storage characteristics. The cyclic-voltammograms exhibit well-defined anodic and cathodic peaks corresponding to the reversible transformation between Ni(OH)$_2$ and NiOOH. The redox peak currents increase proportionally with increasing scan rate, indicating a surface-controlled electrochemical process. Additionally, a slight positive shift in the anodic peak potential and a corresponding negative shift in the cathodic peak potential are observed at

higher scan rates, which can be attributed to the increased polarization and internal resistance of the electrode.

The surface coverage (Γ) of electroactive species on the Ni-based electrode can be estimated from cyclic voltammetry data using the linear relationship between peak current density (i) and scan rate (ν) for a surface-confined redox process. For such systems, the peak current is expressed by the equation:

$$I_{\mathrm{p}} = \frac{(n^2 F^2 A \Gamma \nu)}{4RT} \tag{1}$$

where I_{p} is the peak current (A), n is the number of electrons transferred, F is the Faraday constant, A is the electrode area, Γ is the surface coverage, ν is the scan rate, R is the gas constant, and T is the absolute temperature. The surface coverage can be provided by plotting current density *versus* the scan rate. Whereas, the higher value of surface coverage indicates more active sites available for redox transitions.
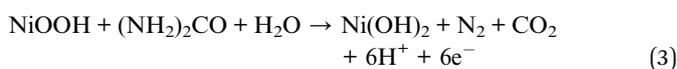
However, the estimated surface coverage for NCO-ZIF-8B was calculated by averaging the anodic and cathodic surface coverage values. The provided surface coverage for NCO-ZIF-8B was 1.9×10^{-8} mol cm^{-2}.

In the oxidation mechanism of urea on Ni-based catalysts, NiOOH acts as the catalytically active species. The oxidation of urea proceeds after Ni(OH)$_2$ is electrochemically transformed into NiOOH, which then oxidizes the urea molecules and regenerated in the redox cycle. As a result, the oxidation of urea on a nickel-based catalyst is proposed to proceed *via* the following mechanism:

(electrochemical activation of nickel-based catalyst)

$$\mathrm{Ni(OH)_2 + OH^- \leftrightarrow NiOOH + H_2O + e^-} \tag{2}$$

(chemical oxidation of urea by NiOOH)

$$\begin{aligned}\mathrm{NiOOH + (NH_2)_2CO + H_2O \rightarrow Ni(OH)_2 + N_2 + CO_2} \\ \mathrm{+ 6H^+ + 6e^-}\end{aligned} \tag{3}$$

As shown in Fig. 5a, the CV profiles of urea electrooxidation were recorded on different electrode surfaces, namely pristine
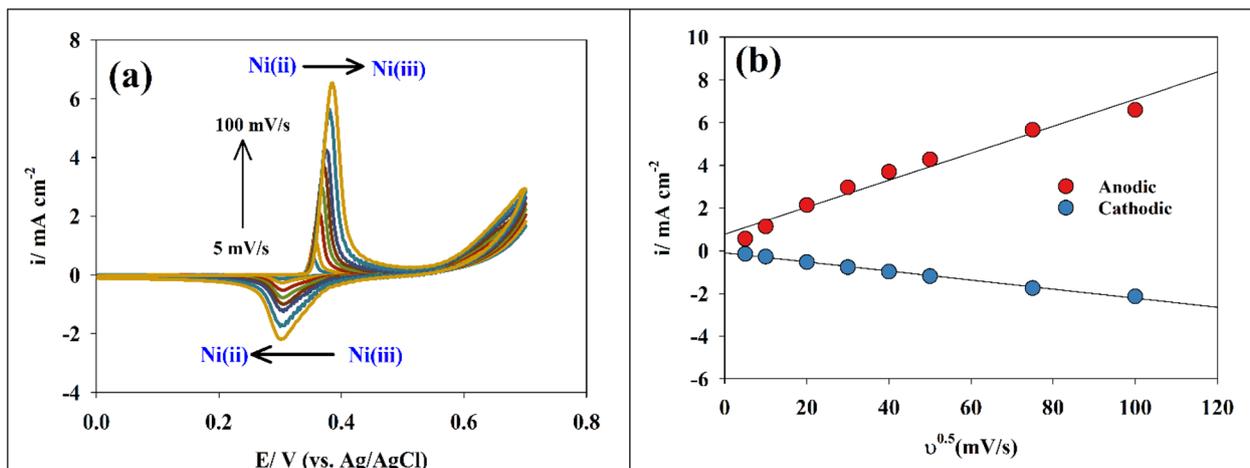

Fig. 4 (a) CVs of NCO–ZIF-8B at various scan rate ranges (5–100 mV s^{-1}), (b) linear relation between scan rate and current density.
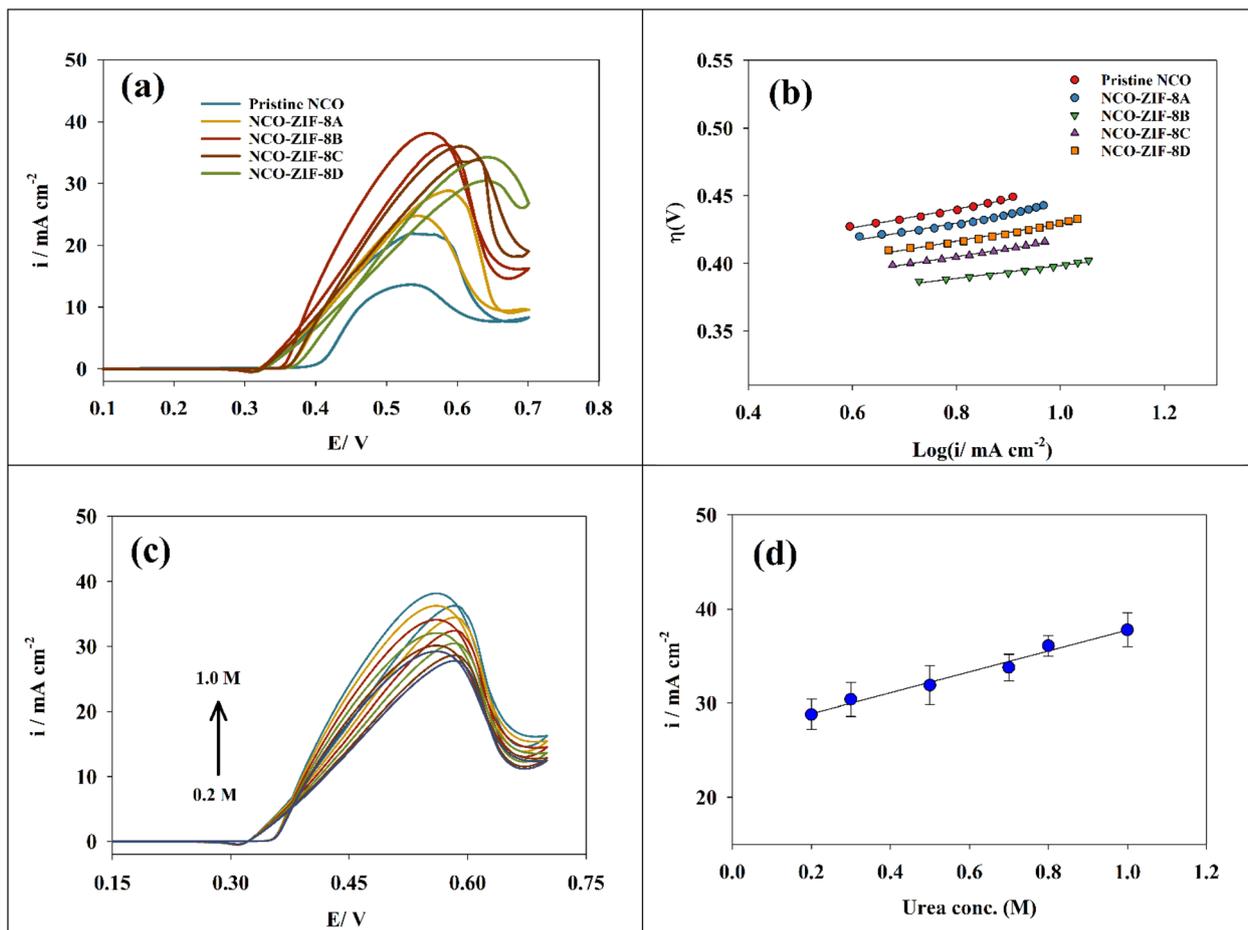
Fig. 5 (a) CV of different surfaces in 1.0 M NaOH and 1.0 M urea, (b) Tafel slope for different surfaces, (c) CV for oxidation of various urea concentration upon NCO–ZIF-8B. (d) Linear relations between urea concentrations and anodic current.

NCO, NCO-ZIF-8A, NCO-ZIF-8B, NCO-ZIF-8C, and NCO-ZIF-8D. Two distinct oxidation peaks appeared around 0.55 V, the first one corresponds to the urea oxidation in the forward scan and the second to the oxidation of CO and other carbonaceous intermediates to carbon dioxide during the reverse scan.[19] Owing to the smaller particle size and larger surface area, the NCO-ZIF-8 composites demonstrated superior catalytic activity toward urea electrooxidation compared with pristine NCO. A detailed comparison, particularly highlighting the performance of NCO-ZIF-8B relative to the other samples, is summarized in Table 1.

A distinct flipping and crossing of the oxidation and reduction branches is observed in the potential range of 0.55–0.65 V (Fig. 4a). This behavior is characteristic of bimetallic hydroxide and oxide systems and reflects the complex redox interplay between the active sites involved in urea electrooxidation

During the forward scan, the anodic current arises mainly from the oxidation of Ni^{2+} to Ni^{3+} and Co^{2+} to Co^{3+}, generating surface NiOOH/CoOOH species that serve as the true active centers for urea oxidation. However, in the reverse scan, partial reduction of these species does not occur at exactly the same potential due to surface reconstruction, adsorbed intermediates, and kinetic asymmetry between oxidation and reduction processes.

The apparent crossing of the curves indicates that the surface is not in a steady state and undergoes potential-

Table 1 Comparison between different surfaces for urea oxidation parameters

Surface	I_P (mA cm^{-2})	E_P(V)	Tafel slope (mV dec^{-1})	Onset potential (V)	Charge transfer coefficient (α)
Pristine-NCO	21.8	0.547	69	0.41	0.145
NCO-ZIF-8A	29.2	0.597	65	0.36	0.154
NCO-ZIF-8B	38.3	0.558	47	0.35	0.213
NCO-ZIF-8C	35.9	0.605	59	0.36	0.170
NCO-ZIF-8D	34.3	0.642	63	0.37	0.159

dependent reorganization. Adsorbed intermediates such as $CO(NH_2)_2$-derived species or carbonate ions may transiently block or modify the active sites, altering the reduction kinetics of Ni^{3+}/Co^{3+} to their lower oxidation states. Similar behavior has been reported for Ni- and Co-based catalysts during urea and alcohol electrooxidation, where dynamic redox transitions cause non-linear CV profiles and curve crossing near the Ni^{2+}/Ni^{3+} redox region. Therefore, the flipping and crossing observed between 0.55 and 0.65 V confirm the reversible but kinetically complex nature of the Ni/Co redox system in alkaline media and highlight the role of surface restructuring in enhancing the urea electrooxidation pathway.

Tafel plots for urea electrooxidation were obtained for pristine NCO, NCO-ZIF-8A, NCO-ZIF-8B, NCO-ZIF-8C, and NCO-ZIF-8D electrodes using quasi-steady-state polarization in a 1.0 M urea + 1.0 M NaOH electrolyte. The relationship between the overpotential and the logarithm of anodic current is depicted in Fig. 5b. The kinetics of the electrode reactions were analyzed according to eqn (4), which is commonly applied in electrochemical studies. The Tafel slope, a key parameter that reflects the electron transfer rate at the electrode–electrolyte interface, was determined to be 69, 65, 47, 59, and 63 mV dec^{-1} for pristine NCO, NCO-ZIF-8A, NCO-ZIF-8B, NCO-ZIF-8C, and NCO-ZIF-8D, respectively. Using the following relation:

$$\text{Tafel slope} = \frac{2.303RT}{\alpha nF} \qquad (4)$$

where F is Faraday's constant, T is the absolute temperature, R is the universal gas constant, and n is the number of electrons involved in the electrooxidation process,

The charge transfer coefficient (α), obtained from the anodic Tafel slopes at 30 °C with $n = 6$, provides important information about the kinetics of the urea oxidation reaction (UOR) on the studied electrodes. The pristine NCO catalyst exhibited a Tafel slope of 69 mV dec^{-1}, corresponding to an α of 0.145, indicating sluggish charge-transfer kinetics. Incorporation of ZIF-8 notably improved the electrochemical behavior, with α values increasing across the modified electrodes. Among them, NCO-ZIF-8B showed the most favorable performance, with the lowest Tafel slope of 47 mV dec^{-1} and the highest α (0.213), signifying a more effective utilization of the applied potential to overcome the activation barrier of the rate-determining step. NCO-ZIF-8C and NCO-ZIF-8D exhibited intermediate behavior, with Tafel slopes of 59 and 63 mV dec^{-1} ($\alpha = 0.170$ and 0.159, respectively), while NCO-ZIF-8A (65 mV dec^{-1}, $\alpha = 0.154$) displayed a modest improvement over pristine NCO. These results confirm that coupling NCO with ZIF-8 enhances the charge-

transfer process during UOR, with the NCO-ZIF-8B electrode delivering the most efficient catalytic kinetics.

Additionally, the urea electrooxidation performance of the NCO-ZIF-8B electrode was examined over a wide range of urea concentrations, from 0.2 M to 1.0 M, in alkaline medium. As presented in Fig. 5c, the anodic peak current consistently increased with rising urea concentration, without any sign of surface saturation within the studied range, furthermore a linear relation is obtained between anodic current density and the urea concentration (see Fig. 5d). This indicates that the active sites on the electrode surface remain accessible even at high urea concentrations, allowing for efficient oxidation kinetics. The absence of saturation behavior reflects a favorable mass transport of urea molecules to the catalyst surface. It suggests that surface coverage effects under these conditions do not limit the catalytic process. Therefore, these characteristics make the electrode highly promising for practical applications where high urea concentrations are encountered, including wastewater treatment processes and direct urea fuel cells (DUFCs), whereas maintaining high current output and catalytic activity is essential for operational efficiency. The comparison between the obtained results and others reported in literature was listed in Table .2.

Linear sweep voltammetry (LSV) was conducted to investigate the urea electrooxidation activity of the NCO-ZIF-8B electrode in 1.0 M NaOH containing urea at scan rates ranging from 5 to 600 mV s^{-1} (see Fig. 6a). The LSV curves exhibit a pronounced increase in anodic current density with increasing scan rate, indicating the enhancement of electrooxidation kinetics at higher sweep speeds. A slight positive shift in the onset and peak potentials is observed with increasing scan rate, which can be attributed to polarization effects and internal resistance. The relationship between peak current (I_p) and scan rate was calculated using the following Randles–Ševčík equation:

$$I_p = 2.99 \times 10^5 \, n(1 - \alpha) \, n_0 \, A \, C_0 \, D^{0.5} \, \nu^{0.5} \qquad (5)$$

where I_p denotes the maximum anodic peak current, n is the total number of electrons transferred in the reaction, n_0 represents the number of electrons involved in the rate-determining step, ν is the scan rate, and C_0 is the urea concentration. The electrode surface area was 0.0707 cm^2, while the diffusion coefficient (D, in $cm^2 \, s^{-1}$) was obtained from the slope of the linear plot of I_p versus $\nu^{1/2}$, as presented in Fig. 6b, according to the Randles–Ševčík equation. The analysis confirms that all synthesized electrocatalysts exhibit diffusion-controlled

Table 2 Comparison table between different modified surfaces for UEO

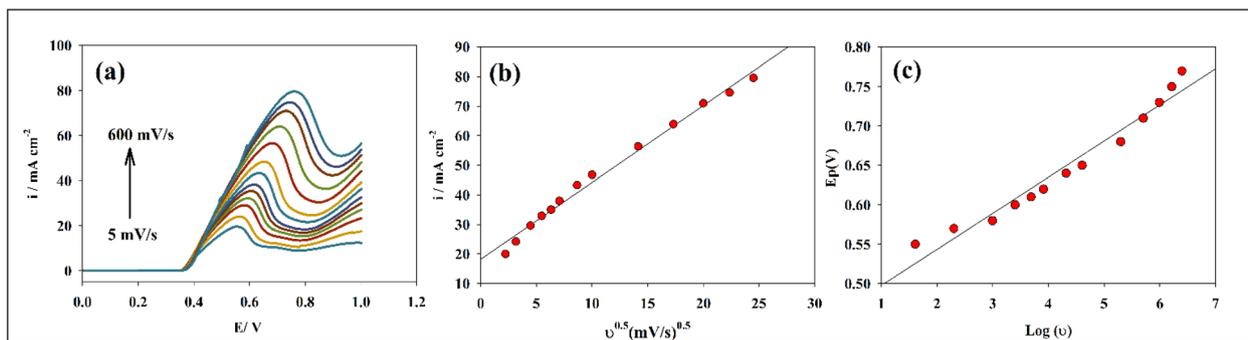| Surface	Urea conc. (M)	[OH] conc. (M)	Scan rate (mV s^{-1})	Current density (mA cm^{-2})	References
NCO-ZIF-8B	1.0	1.0	20	39	This work
NiCo$_2$O$_4$@chitosan	1.0	1.0	20	43	66
Ni$_{0.8}$5Se/rGO	0.5	1.0	50	10	67
Ni$_{0.9}$Cu$_{0.1}$	0.3	0.5	20	32	19
NiO–MnO$_x$/polyaniline	0.3	0.5	20	16	68

Fig. 6 (a) LSV for modified NCO-ZIF-8B for range of scan rates. (b) Relation between square root of the scan rate and urea oxidation current. (c) Linear relation between logarithm of scan rate *versus* peak potential.

kinetics for urea oxidation. For the NCO-ZIF-8B electrode, the calculated diffusion coefficient was 1.24×10^{-4} cm^2 s^{-1}.

Since the reaction is irreversible, the kinetic parameters were further evaluated using Laviron's equation for irreversible systems:

$$E_{\mathrm{p}} = E^{\circ} + \frac{2.302RT}{\alpha nF}\log\left(\frac{RTk^{\circ}}{\alpha nF}\right) - \frac{2.302RT}{\alpha nF}\log v \qquad (6)$$

where E_{p} represents the anodic peak potential, E° is the formal potential, α is the electron transfer coefficient, and k° is the standard heterogeneous rate constant. The relationship between E_{p} and log v can be used to extract both α and k°, thereby providing insight into the charge-transfer kinetics. As illustrated in Fig. 6c, a linear dependence of E_{p} on log v was observed for urea oxidation. Based on the slope and assuming a six-electron transfer process ($n = 6$), the electron transfer coefficient (α) was determined to be 0.219, which is consistent with the value obtained from the Tafel slope analysis. Furthermore, the standard heterogeneous rate constant (k°) was estimated from the intercept of the ln v versus E_{p} plot, considering a formal potential of $E^{\circ} = 0.58$ V (*vs.* Ag/AgCl). The calculated k° was 1.2×10^{-4} s^{-1}. Overall, the combined evaluation using the Randles–Sevcik and Laviron equations indicates that urea electrooxidation on NCO-ZIF-8B follows a mixed mechanism,

characterized by fast electron transfer through the Ni(OH)$_2$/NiOOH redox couple alongside efficient diffusion of urea molecules from the bulk solution to the electrode surface.

Electrochemical impedance spectroscopy (EIS) was performed on the different electrodes to evaluate how surface composition influences urea electrooxidation (UEO) and charge transfer characteristics. As the represented in Fig. 7a, Nyquist plot of NCO-ZIF-8B in a solution of 1.0 M urea at different potential ranges from 0.4 to 0.8 V (*vs.* Ag/AgCl). For a potential range from 0.6 to 0.8 V, the data was fitted to circuit #1 as represented in the inset of Fig. 7a. The solution resistance (R_{s}) is connected in series with the charge transfer resistance (R_1) and the constant phase element (CPE), which are arranged in parallel. Furthermore, R_1 is linked to an additional branch consisting of R_2 and CPE2, also connected in parallel. In contrast, the Nyquist data at potentials of 0.4 and 0.5 V can be fitted to an equivalent circuit consisting of the solution resistance (R_{s}) in series with two parallel RC branches, each comprising a resistor (R) and a constant phase element (CPE) (see fitting circuit #2). The fitting data for different potentials are listed in Table 3.

Furthermore, the effect of urea concentration was investigated using EIS data. Fig. 7b shows the Nyquist plot for modified GC/NCO-ZIF-8B in different urea concentrations at a potential of
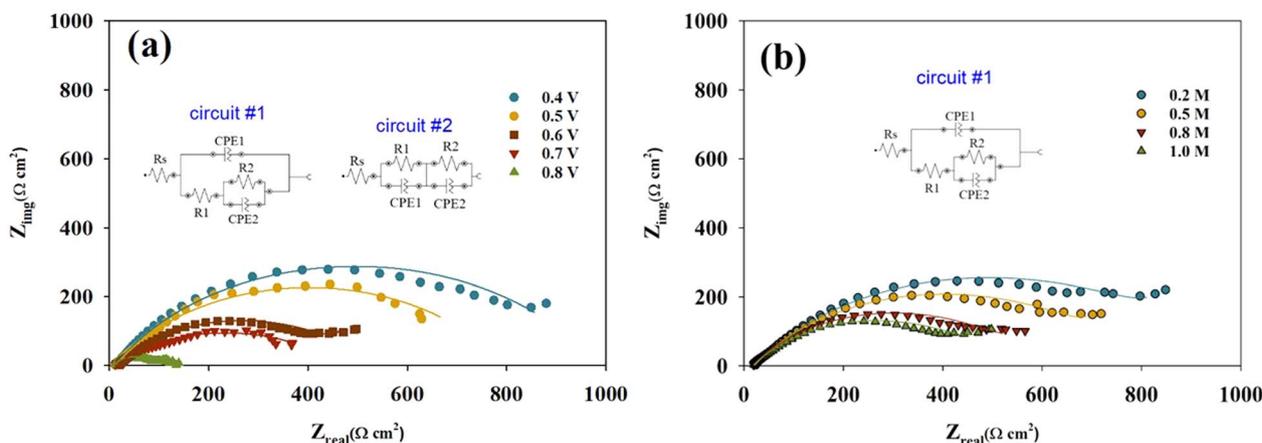

Fig. 7 Nyquist plot for NCO-ZIF-8B (a) at different potentials, (b) different urea concentrations.

Table 3 Fitting parameters for modified NCO–ZIF–8B at different potentials

| Potential (V) | R_s Ω cm^2 | R_1 Ω cm^2 | CPE1 | | R_2 Ω cm^2 | CPE2 | |
			Y_0	n		Y_0	n
0.4	11.2	318	0.000021	0.571	855	0.00104	0.514
0.5	11.1	243	0.000031	0.612	667	0.00301	0.601
0.6	11.3	134	0.000044	0.619	460	0.00319	0.681
0.7	9.4	95	0.000047	0.622	367	0.00498	0.445
0.8	10.1	68	0.000075	0.751	135	0.00547	0.532

Table 4 Fitting parameters for modified NCO–ZIF–8B in different urea concentrations

| Concentration (M) | R_s Ω cm^2 | R_1 Ω cm^2 | CPE1 | | R_2 Ω cm^2 | CPE2 | |
			Y_0	N		Y_0	N
0.2	14.7	450	0.000034	0.611	870	0.00277	0.591
0.5	12.4	421	0.000037	0.677	732	0.00285	0.628
0.8	11.9	367	0.000041	0.683	510	0.00291	0.641
1.0	11.3	134	0.000044	0.711	460	0.00319	0.681

0.6 V. The Nyquist plot diameter was observed to decrease with increasing urea concentration due to the increased charge transfer process. The fitting circuit #1 represents the fitted data, as illustrated in the inset of Fig. 6b. The fitted data for different urea concentrations are summarized in Table 4.

The EIS results confirm that increasing potential and urea concentration significantly lowers charge transfer resistances and enhances the electrode's pseudocapacitive behavior. The progressive increase in CPE exponents indicates a transition toward more ideal capacitive behavior associated with improved surface utilization and reaction kinetics. These findings demonstrate that the modified NCO-ZIF-8B electrode exhibits efficient charge transport and strong pseudocapacitive contributions, crucial for effective urea electrooxidation.

Stability enhancement is a primary goal in catalyst design, as it determines the long-term applicability of electrocatalysts in direct urea fuel cells and wastewater treatment. To assess durability, the long-term stability of the prepared electrodes with different ratios of nickel cobaltite (NCO) and ZIF-8 electrocatalysts was evaluated through chronoamperometric measurements at 0.6 V in 1.0 M NaOH solution containing 1.0 M urea, as presented in Fig. 8. Chronoamperometry tests were conducted for 10 hours on pristine NCO, and different samples of NCO-ZIF-8 electrodes. The percentage loss in electrode activity was determined to be approximately 14.2%, 10.5%, 9.2%, 12.5%, and 11.8% for pristine NCO, NCO-ZIF-8A, NCO-ZIF-8B, NCO-ZIF-8C, and NCO-ZIF-8D electrodes, respectively. The relatively lower decay in current density for the NCO-ZIF-8 modified electrodes compared to pristine NCO indicates that the incorporation of ZIF-8 significantly improves electrode stability. Among all the samples, NCO-ZIF-8B exhibited the best performance with 9.2% current decay, suggesting that it is the optimized NCO-to-ZIF-8 ratio which provides enhanced durability by reducing active site blockage and mitigating catalyst deactivation. The improved stability can be attributed to the synergistic effect between NCO and ZIF-8, where the porous structure of ZIF-8 not only facilitates efficient diffusion of reactants and products but also acts as a protective matrix, preventing agglomeration and structural collapse of NCO nanoparticles during prolonged electrolysis. The gradual activity loss observed for all electrodes can be ascribed to the accumulation of intermediate species such as carbonate on active sites, a common deactivation pathway in urea electrooxidation. Nevertheless, the relatively low decay values highlight the robustness of the NCO-ZIF-8 system compared to pristine NCO and confirm its potential for practical applications requiring extended operation times.
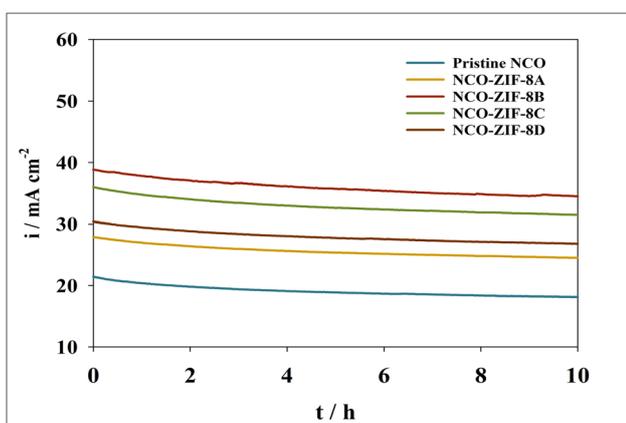
4 Conclusion

A series of nickel cobaltite-ZIF-8 nanocomposites with different ratios between NCO and ZIF-8 were successfully synthesized and evaluated as electrocatalysts for urea electrooxidation in

Fig. 8 Chronoamperograms of different modified electrodes in the presence of 1.0 M urea and 1.0 M NaOH.

alkaline media. Structural and electrochemical analyses confirmed that the integration of ZIF-8 with NCO significantly enhanced catalytic performance compared to pristine NCO. The optimized nanocomposite, NCO-ZIF-8B, exhibited the highest electrocatalytic activity, demonstrating superior current density, lower onset potential, and favorable Tafel slope, which can be attributed to the synergistic interaction between the highly conductive NCO and the porous ZIF-8 framework. In addition, long-term stability measurements revealed that NCO-ZIF-8B retained most of its activity with only ~9.2% current decay over 10 hours, outperforming pristine NCO and other composite ratios. The improved durability is primarily ascribed to the protective and dispersive role of ZIF-8, which enhances mass transport, prevents nanoparticle agglomeration, and mitigates active site poisoning during urea electrooxidation. Finally, these findings highlight the promise of NCO-ZIF-8 composites as efficient and durable electrocatalysts for direct urea fuel cells and wastewater treatment applications. Future work should focus on tailoring the pore structure and electronic properties of ZIF-based frameworks and exploring multi-metallic or heteroatom-doped architectures to further enhance catalytic activity and long-term operational stability.

Author contributions

Conceptualization, S. S. M. and M. A. H.; methodology, S. S. M. and M. A. H.; software, F. S. A., S. S. M. and M. A. H.; validation, S. S. M. and M. A. H.; formal analysis, S. S. M. and M. A. H.; investigation, F. S. A., S. S. M., N. S. A.-K., and H. A. A.; resources, F. S. A., S. S. M., N. S. A.-K. and H. A. A.; data curation, S. S. M. and M. A. H.; writing—original draft, M. A. H.; writing—review & editing, S. S. M., H. A. A. and M. A. H.; visualization, M. A. H.; supervision, F. S. A., S. S. M., N. S. A.-K. and H. A. A.; project administration, F. S. A., N. S. A.-K. and H. A. A.; funding acquisition, F. S. A, N. S. A.-K. and H. A. A., all authors have read and agreed to the published version of the manuscript.

Conflicts of interest

The authors declare that there is no conflict of interest regarding the publication of this paper.

Data availability

The datasets used and analyzed during the current study are available from the corresponding author upon reasonable request.

Acknowledgements

References

1 R. C. Dorf, *Technology, Humans, and Society: toward a Sustainable World*, Elsevier, 2001.

2 V. Balzani and N. Armaroli, *Energy for a Sustainable World: from the Oil Age to a Sun-Powered Future*, John Wiley & Sons, 2010.

3 A. M. Omer, Energy, environment and sustainable development, *Renewable Sustainable Energy Rev.*, 2008, **12**, 2265–2300.

4 N. L. Panwar, S. C. Kaushik and S. Kothari, Role of renewable energy sources in environmental protection: a review, *Renewable Sustainable Energy Rev.*, 2011, **15**, 1513–1524.

5 S. Chu and A. Majumdar, Opportunities and challenges for a sustainable energy future, *Nature*, 2012, **488**, 294–303.

6 M. J. B. Kabeyi and O. A. Olanrewaju, Sustainable energy transition for renewable and low carbon grid electricity generation and supply, *Front. energy res.*, 2022, **9**, 743114.

7 A. Nautiyal and A. Ramlal, Clean Energy Sources for a better and sustainable environment of future generations, *Energy: Crisis, Challenges and Solutions*, 2021, 151–168, DOI: **10.1002/9781119741503.ch8**.

8 S. Agrawal and R. Soni, Sources, Importance and Prospects for Sustainable Future, *Renewable Energy*, 2021, 131–150, DOI: **10.1002/9781119741503.ch7**.

9 N. S. Al-Kadhi, M. A. Hefnawy, S. S. Nafee, F. S. Alamro, R. A. Pashameah, H. A. Ahmed and S. S. Medany, Zinc Nanocomposite Supported Chitosan for Nitrite Sensing and Hydrogen Evolution Applications, *Polymers*, 2023, 2357, DOI: **10.3390/POLYM15102357**.

10 M. A. Hefnawy, A. Nafady, S. K. Mohamed and S. S. Medany, Facile green synthesis of Ag/carbon nanotubes composite for efficient water splitting applications, *Synth. Met.*, 2023, **294**, 117310, DOI: **10.1016/J.SYNTHMET.2023.117310**.

11 W. Shafik, Introduction to Renewable Energy Technologies, *Soft Computing in Renewable Energy Technologies*, 2024, pp. 1–31, DOI: **10.1201/9781003462460-1**.

12 K. A. Naveen Kumar and A. Vigneshwaran, *Renewable Energy Resources and Their Types*, pp. 116–135, DOI: **10.4018/978-1-6684-8816-4.CH008**, **https://Services.Igi-Global.Com/Resolvedoi/Resolve.Aspx?Doi=10.4018/978-1-6684-8816-4.Ch008**.

13 A. Kumar, D. B. Pal, Renewable Energy Development Sources and Technology: overview, *Renewable Energy Development: Technology, Material and Sustainability*, 2025, pp. 1–23, DOI: **10.1007/978-981-97-9626-7_1**.

14 U. Lucia, Overview on fuel cells, *Renewable Sustainable Energy Rev.*, 2014, **30**, 164–169, DOI: **10.1016/j.rser.2013.09.025**.

15 S. Kartha and P. Grimes, Fuel Cells: Energy Conversion for the Next Century, *Phys. Today*, 1994, **47**, 54–61, DOI: **10.1063/1.881426**.

16 J. Martins and F. P. Brito, Alternative Fuels for Internal Combustion Engines, *Energies*, 2020, 4086, DOI: **10.3390/EN13164086**.

17 A. Boudghene Stambouli and E. Traversa, Fuel cells, an alternative to standard sources of energy, *Renewable Sustainable Energy Rev.*, 2002, **6**, 295–304, DOI: 10.1016/S1364-0321(01)00015-6.

18 M. A. Hefnawy, S. S. Medany, R. M. El-Sherif, N. El-Bagoury and S. A. Fadlallah, High-performance IN738 superalloy derived from turbine blade waste for efficient ethanol, ethylene glycol, and urea electrooxidation, *J. Appl. Electrochem.*, 2023, **53**, 1337–1348, DOI: 10.1007/S10800-023-01862-7/FIGURES/6.

19 M. A. Hefnawy, S. A. Fadlallah, R. M. El-Sherif and S. S. Medany, Synergistic effect of Cu-doped NiO for enhancing urea electrooxidation: Comparative electrochemical and DFT studies, *J. Alloys Compd.*, 2022, **896**, 162857, DOI: 10.1016/J.JALLCOM.2021.162857.

20 S. Goswami, S. J. Phukan, G. Gupta, R. K. Pai, S. Rana, M. Roy, P. Kumar and S. Garai, Direct Urea Fuel Cells: A Review on Roadmap, Mechanism, Bottleneck, and Future Perspective, *Energy Fuels*, 2025, **39**, 6709–6727, DOI: 10.1021/ACS.ENERGYFUELS.4C05534.

21 W. Xu, Z. Wu and S. Tao, Urea-Based Fuel Cells and Electrocatalysts for Urea Oxidation, *Energy Technol.*, 2016, **4**, 1329–1337, DOI: 10.1002/ENTE.201600185.

22 J. Zhang, Y. Tan and W.-J. Song, Zeolitic imidazolate frameworks for use in electrochemical and optical chemical sensing and biosensing: a review, *Microchim. Acta*, 2020, **187**, 234.

23 K. Noh, J. Lee and J. Kim, Compositions and structures of zeolitic imidazolate frameworks, *Isr. J. Chem.*, 2018, **58**, 1075–1088.

24 A. Subhadarshini and B. Nanda, Zeolitic imidazolium framework (ZIF-8) and their derivative-based material for antibacterial study: a comprehensive review, *Discover Mater.*, 2025, **5**, 1–22.

25 R. Perveen, S. Bibi, M. A. Salem, M. H. Helal, A. Afzal, M. A. Wattoo and A. U. Rehman, Recent progress in ZIF-polymer composites for advanced drug delivery applications, *J. Mater. Chem. B*, 2025, **13**, 6949–6989, DOI: 10.1039/D5TB00147A.

26 J. Troyano, A. Carné-Sánchez, C. Avci, I. Imaz and D. Maspoch, Colloidal metal–organic framework particles: the pioneering case of ZIF-8, *Chem. Soc. Rev.*, 2019, **48**, 5534–5546.

27 G. Zhong, D. Liu and J. Zhang, The application of ZIF-67 and its derivatives: adsorption, separation, electrochemistry and catalysts, *J. Mater. Chem. A*, 2018, **6**, 1887–1899.

28 Q. Shi, Z. Chen, Z. Song, J. Li and J. Dong, Synthesis of ZIF-8 and ZIF-67 by steam-assisted conversion and an investigation of their tribological behaviors, *Angew. Chem., Int. Ed.*, 2011, **50**, 672–675.

29 Y. Ding, H. Wang, M. Yu, W. Zheng, X. Ruan, X. Li, Y. Xi, Y. Dai, H. Liu and G. He, Amine group graft ZIF-93 to create gas storage space to improve the gas separation performance of Pebax-1657 MMMs, *Sep. Purif. Technol.*, 2023, **309**, 122949.

30 L. Mu, B. Liu, H. Liu, Y. Yang, C. Sun and G. Chen, A novel method to improve the gas storage capacity of ZIF-8, *J. Mater. Chem.*, 2012, **22**, 12246–12252.

31 A. Thomas and M. Prakash, The role of binary mixtures of ionic liquids in ZIF-8 for selective gas storage and separation: a perspective from computational approaches, *J. Phys. Chem. C*, 2020, **124**, 26203–26213.

32 Y. Huang, X. Zeng, L. Guo, J. Lan, L. Zhang and D. Cao, Heavy metal ion removal of wastewater by zeolite-imidazolate frameworks, *Sep. Purif. Technol.*, 2018, **194**, 462–469.

33 H. Ukani, S. Mehra, B. Parmar, A. Kumar, I. Khan, O. A. El Seoud and N. Malek, Metal–organic framework-based aerogel: a novel adsorbent for the efficient removal of heavy metal ions and selective removal of a cationic dye from aqueous solution, *Ind. Eng. Chem. Res.*, 2023, **62**, 5002–5014.

34 J. Zakzeski, A. Dębczak, P. C. A. Bruijnincx and B. M. Weckhuysen, Catalytic oxidation of aromatic oxygenates by the heterogeneous catalyst Co-ZIF-9, *Appl. Catal., A*, 2011, **394**, 79–85.

35 J. Zakzeski, A. Dębczak, P. C. A. Bruijnincx and B. M. Weckhuysen, Catalytic oxidation of aromatic oxygenates by the heterogeneous catalyst Co-ZIF-9, *Appl. Catal., A*, 2011, **394**, 79–85.

36 S. Dutta, Z. Liu, H. Han, A. Indra and T. Song, Electrochemical energy conversion and storage with zeolitic imidazolate framework derived materials: a perspective, *ChemElectroChem*, 2018, **5**, 3571–3588.

37 D. Yu, Q. Shao, J. Wang, Y. Zhang, Y. Wang, J. Liu, J. Cui and Y. Wu, Controllable and high-yielding synthesis of ZIF-8 hollow structures for electrochemical energy storage, *Chem. Eng. J.*, 2022, **431**, 134008.

38 B. Y. Guan, X. Y. Yu, H. Bin Wu and X. W. Lou, Complex nanostructures from materials based on metal–organic frameworks for electrochemical energy storage and conversion, *Adv. Mater.*, 2017, **29**, 1703614.

39 D. Behera, P. Priyadarshini and K. Parida, ZIF-8 metal–organic frameworks and their hybrid materials: emerging photocatalysts for energy and environmental applications, *Dalton Trans.*, 2025, **54**, 2681–2708.

40 T. V. M. Sreekanth, X. Wei, K. Yoo and J. Kim, Urea electrooxidation using ZIF-67-derived Co_3O_4 catalyst, *Mater. Chem. Phys.*, 2023, **295**, 127167.

41 A. H. Bashal, M. A. Hefnawy, H. A. Ahmed, M. A. El-Atawy, R. A. Pashameah and S. S. Medany, Green synthesis of $NiFe_2O_4$ nano-spinel oxide-decorated carbon nanotubes for efficient capacitive performance—Effect of electrolyte concentration, *Nanomaterials*, 2023, **13**, 2643.

42 F. S. Alamro, M. A. Hefnawy, N. S. Al-Kadhi, A. M. Mostafa, M. M. Motawea, H. A. Ahmed, A. S. Alshomrany and S. S. Medany, Synthesis of spinel Nickel Ferrite ($NiFe_2O_4$)/CNT electrocatalyst for ethylene glycol oxidation in alkaline medium, *Heliyon*, 2024, **10**(16), e35791, DOI: 10.1016/j.heliyon.2024.e35791.

43 M. A. Hefnawy, R. Abdel-Gaber, S. M. Gomha, M. E. A. Zaki and S. S. Medany, Synthesis of Nickel-Manganese Spinel

Oxide Supported on Carbon-Felt Surface to Enhance Electrochemical Capacitor Performance, *Electrocatalysis*, 2025, **16**, 500–512, DOI: 10.1007/s12678-025-00932-y.

44 N. E. A. El-Gamel, S. S. Medany and M. A. Hefnawy, Synthesis of NiCo$_2$O$_4$ supported on Chitosan for potential adsorption of copper ions in water samples, *Sci. Rep.*, 2025, **15**, 14402, DOI: 10.1038/s41598-025-96777-y.

45 F. S. Alamro, S. S. Medany, N. S. Al-Kadhi, A. M. Mostafa, W. F. Zaher, H. A. Ahmed and M. A. Hefnawy, Controllable synthesis of Fe$_2$O$_3$/nickel cobaltite electrocatalyst to enhance oxidation of small molecules, *Catalysts*, 2024, **14**, 329.

46 B. Saravanakumar, G. Ravi, V. Ganesh, R. K. Guduru and R. Yuvakkumar, MnCo$_2$O$_4$ nanosphere synthesis for electrochemical applications, *Mater. Sci. Energy Technol.*, 2019, **2**, 130–138.

47 S. Meeran, A. A. S. Begum, H. M. K. Sheit, M. K. V. Mohamed and K. S. Mohan, The deep investigation of structural and electrochemical analysis on the anti-corrosion behavior of MgCo$_2$O$_4$ and ZnCo$_2$O$_4$ spinel nanoparticles in acid medium, *Results Surf. Interf.*, 2025, **18**, 100416.

48 A. de A. Lourenço, R. A. Raimundo, R. F. Alves, R. B. da Silva, D. A. Macedo and F. F. da Silva, Impregnation of metal ions on ZIF-67 towards the production of mixed-metals spinels for OER electrocatalysis, *J. Solid State Chem.*, 2025, **348**, 125352, DOI: 10.1016/J.JSSC.2025.125352.

49 Z. Wang, C. Lai, L. Qin, Y. Fu, J. He, D. Huang, B. Li, M. Zhang, S. Liu, L. Li, W. Zhang, H. Yi, X. Liu and X. Zhou, ZIF-8-modified MnFe$_2$O$_4$ with high crystallinity and superior photo-Fenton catalytic activity by Zn–O–Fe structure for TC degradation, *Chem. Eng. J.*, 2020, **392**, 124851, DOI: 10.1016/J.CEJ.2020.124851.

50 D. Wang, Z. Cuo and Y. Chen, ZIF-67 derived lamellar nanoarray spinel as effective catalyst for toluene combustion, *Mater. Lett.*, 2023, **345**, 134482, DOI: 10.1016/J.MATLET.2023.134482.

51 D. Yang, W. Qiu, J. Xu, P. Wang, D. Jin, X. Peng, B. Hong, H. Jin, H. Ge and X. Wang, Facilely synthesized NiCo$_2$O$_4$/CNTs nanocomposites for surpercapacitors with enhanced performance, *Int. J. Electrochem. Sci.*, 2016, **11**, 7262–7268.

52 Y. Li and X. Wu, Fabrication of urchin-like NiCo$_2$O$_4$ microspheres assembled by using SDS as soft template for anode materials of Lithium-ion batteries, *Ionics*, 2018, **24**, 1329–1337.

53 H. Gharibi, Z. Pazhand, M. M. Taghiabadi, S. Javadian, R. Sabbaghi and S. M. S. Bagheri, Achieving high capacity by controlling the size of Fe/Co–N–C(t) in the cathode of lithium-oxygen batteries, *Appl. Surf. Sci.*, 2025, **680**, 161346, DOI: 10.1016/j.apsusc.2024.161346.

54 X. Gao, X. Hou, Z. Ma, C. Xiao and L. Jia, Highly dispersed Ag nanocrystals functionalized ZIF-8 derived ZnO hollow structures for superior sensitive and selective detection of nitric oxide, *Sens. Actuators, B*, 2025, **422**, 136646, DOI: 10.1016/j.snb.2024.136646.

55 S. Goyal, M. S. Shaharun, C. F. Kait and B. Abdullah, Effect of monometallic copper on zeolitic imidazolate framework-8 synthesized by hydrothermal method, *J. Phys.:Conf. Ser.*, 2018, **1123**, 012062, DOI: 10.1088/1742-6596/1123/1/012062.

56 X. Lin, M. Huang, T. Lu, W. Zhao, C. Hu, X. Gu and W. Zhang, Characterization of Imidazole Compounds in Aqueous Secondary Organic Aerosol Generated from Evaporation of Droplets Containing Pyruvaldehyde and Inorganic Ammonium, *Atmosphere*, 2022, **13**, 970, DOI: 10.3390/ATMOS13060970.

57 B. Hachuła, M. Nowak and J. Kusz, Crystal and molecular structure analysis of 2-methylimidazole, *J. Chem. Crystallogr.*, 2010, **40**, 201–206, DOI: 10.1007/S10870-009-9634-9/FIGURES/4.

58 M.-T. Forel, M.-L. Josien and N. Fuson, Infrared Band Assignments for the 2900 cm^{-1} Region Methyl Group Vibrations in XC$_6$H$_4$COOCH$_3$, XC$_6$H$_4$CH$_3$, and XC$_6$H$_4$COCH$_3$ Molecules, *JOSA*, 1960, **50**(12), 1228–1231, DOI: 10.1364/JOSA.50.001228.

59 Y. Wu, X. Song, S. Xu, J. Zhang, Y. Zhu, L. Gao and G. Xiao, 2-Methylimidazole Modified Co-BTC MOF as an Efficient Catalyst for Chemical Fixation of Carbon Dioxide, *Catal. Lett.*, 2019, **149**, 2575–2585, DOI: 10.1007/S10562-019-02874-9/FIGURES/11.

60 D. M. L. Goodgame, M. Goodgame and G. W. Rayner-Canham, Spectroscopic studies of substituted imidazole complexes. I. Some complexes of 2-methylimidazole, *Inorg. Chim. Acta*, 1969, **3**, 399–405, DOI: 10.1016/S0020-1693(00)92520-9.

61 A. H. A. Rahim, S. N. F. Yusuf, S. R. Majid and Z. Osman, One-step co-precipitated β-Ni(OH)$_2$ at different ratios of Ni/2-methylimidazole and its energy storage behaviour, *J. Appl. Electrochem.*, 2022, **52**, 159–172, DOI: 10.1007/S10800-021-01627-0/METRICS.

62 J. Liu, J. He, L. Wang, R. Li, P. Chen, X. Rao, L. Deng, L. Rong and J. Lei, NiO-PTA supported on ZIF-8 as a highly effective catalyst for hydrocracking of Jatropha oil, *Sci. Rep.*, 2016, **6**, 1–11, DOI: 10.1038/SREP23667.

63 M. Attwa, A. Said, M. ElGamal, Y. El-Shaer and S. Elbasuney, Bespoke Energetic Zeolite Imidazolate Frameworks-8 (ZIF-8)/Ammonium Perchlorate Nanocomposite: A Novel Reactive Catalyzed High Energy Dense Material with Superior Decomposition Kinetics, *J. Inorg. Organomet. Polym. Mater.*, 2024, **34**, 387–400, DOI: 10.1007/S10904-023-02834-2/FIGURES/18.

64 M. Adnan, K. Li, L. Xu and Y. Yan, X-Shaped ZIF-8 for Immobilization Rhizomucor miehei Lipase *via* Encapsulation and Its Application toward Biodiesel Production, *Catalysts*, 2018, **8**, 96, DOI: 10.3390/CATAL8030096.

65 J. Ran, H. Chen, S. Bi, Q. Guo, Z. Deng, G. Cai, D. Cheng, X. Tang and X. Wang, One-step in-situ growth of zeolitic imidazole frameworks-8 on cotton fabrics for photocatalysis and antimicrobial activity, *Cellulose*, 2020,

27, 10447–10459, DOI: **10.1007/S10570-020-03483-1/FIGURES/9**.

66 F. S. Alamro, M. A. Hefnawy, S. S. Nafee, N. S. Al-Kadhi, R. A. Pashameah, H. A. Ahmed and S. S. Medany, Chitosan Supports Boosting $NiCo_2O_4$ for Catalyzed Urea Electrochemical Removal Application, *Polymers*, 2023, **15**, 3058, DOI: **10.3390/POLYM15143058**.

67 L. Zhao, Y. Chang, M. Jia, J. Jia and Z. Wen, Monodisperse Ni0·85Se nanocrystals on rGO for high-performance urea electrooxidation, *J. Alloys Compd.*, 2021, **852**, 156751, DOI: **10.1016/J.JALLCOM.2020.156751**.

68 M. A. Hefnawy, S. S. Medany, R. M. El-Sherif and S. A. Fadlallah, $NiO–MnO_x$/Polyaniline/Graphite Electrodes for Urea Electrocatalysis: Synergetic Effect between Polymorphs of MnO_x and NiO, *ChemistrySelect*, 2022, **7**, e202103735, DOI: **10.1002/SLCT.202103735**.